Earth-Viewing L-Band Radiometer Sensing of Sea Surface Scattered Celestial Sky Radiation—Part II: Application to SMOS

Nicolas Reul, Joseph Tenerelli, Nicolas Floury, and Bertrand Chapron

***Abstract*—We examine how the rough sea surface scattering of L-band celestial sky radiation might affect the measurements of the future European Space Agency Soil Moisture and Ocean Salinity (SMOS) mission. For this purpose, we combined data from several surveys to build a comprehensive all-sky L-band celestial sky brightness temperature map for the SMOS mission that includes the continuum radiation and the hydrogen line emission rescaled for the SMOS bandwidth. We also constructed a separate map of strong and very localized sources that may exhibit L-band brightness temperatures exceeding 1000 K. Scattering by the roughened ocean surface of radiation from even the strongest localized sources is found to reduce the contributions from these localized strong sources to negligible levels, and rough surface scattering solutions may be obtained with a map much coarser than the original continuum maps. In rough ocean surface conditions, the contribution of the scattered celestial noise to the reconstructed brightness temperatures is not significantly modified by the synthetic antenna weighting function, which makes integration over the synthetic beam unnecessary. The contamination of the reconstructed brightness temperatures by celestial noise exhibits a strong annual cycle with the largest contamination occurring in the descending swaths in September and October, when the specular projection of the field of view is aligned with the galactic equator. Ocean surface roughness may alter the contamination by over 0.1 K in 30% of the SMOS measurements. Given this potentially large impact of surface roughness, an operational method is proposed to account for it in the SMOS level 2 sea surface salinity algorithm.**

***Index Terms*—Microwave radiometry, sea surface electromagnetic scattering.**

I. Introduction

CELESTIAL sky L-band radiation scattered by the ocean surface can contaminate spaceborne measurements of upwelling sea surface brightness temperature used to retrieve sea surface salinity (SSS). The sensitivity of the linearly polarized sea surface brightness temperature to salinity ranges from about 0.2 to 0.8 K/psu [1] (depending on ocean surface temperature, incidence angle, and polarization). Since the open ocean surface salinity generally ranges from 32 to 37 psu, the expected dynamical range of L-band emission brightness temperatures associated with variations in SSS alone is small relative to the total brightness temperature, which is less than approximately 4 K for open ocean conditions.

For the Aquarius/SAC-D mission, it was reported in [2] that, under the assumption of a flat perfectly conducting Earth surface (with a reflectivity of 1), the total celestial sky radiation contribution to the antenna temperature varies from a little less than 4 K to more than 9 K. For a perfectly flat dielectric sea surface, the reflectivity may range from about 30% to 80% at 1.4 GHz for incidence angles below 50°, depending on the SSS, sea surface physical temperature, and observation polarization. In this case, the contamination ranges from about 1 to 7 K. As discussed in [3] (hereinafter referred to as Part I), ocean surface roughness both decreases the surface reflectivity and directionally spreads the impact of the source brightness. For specular points in the vicinity of the galactic equator, the spreading effect of the rough surface greatly reduces the impact along the equator and broadens the contamination far beyond the narrow bright source concentrated along the equator. Nevertheless, for specular points far from strong sources, sea surface roughness has a negligible impact on the reflected signal. Overall, the intensity of the scattered celestial noise ranges from approximately 30% to 70% of the flat ocean surface reflected values, with most of the variation associated with the directional spreading of the radiation.

The nonuniform distribution of celestial radiation has an important systematic impact on the measurements. The future European Space Agency Soil Moisture and Ocean Salinity (SMOS) and National Aeronautics and Space Administration/Comisión Nacional de Actividades Espaciales Aquarius/SAC-D satellites that are dedicated to SSS remote sensing will be launched in the near future into sun-synchronous orbits, and considering these orbits along with the Earth's orbit around the sun, the celestial sky glitter contamination will exhibit strong geographic and seasonal dependence. As such, flagging and correction strategies for such contamination must be developed to reduce large-scale seasonal and geographical biases in the retrieved surface salinity fields.

To achieve the 0.1-psu accuracy goal for the retrieved salinity, the sky glitter contribution must be estimated with an uncertainty not exceeding 0.05 K. This is a stringent constraint that may be difficult to satisfy given the accuracies of both the future SMOS radiometric measurements and the sky brightness

Manuscript received March 1, 2007; revised June 20, 2007.

N. Reul, J. Tenerelli, and B. Chapron are with the Laboratoire d'Océanographie Spatiale, Institut Français de Recherche et d'Exploitation de la Mer, 29280 Brest, France (e-mail: nreul@ifremer.fr).

N. Floury is with the Electromagnetics and Space Environments Division, European Space Research and Technology Centre (ESTEC), European Space Agency, 2200 AG Noordwijk, The Netherlands.

Color versions of one or more of the figures in this paper are available online at http://ieeexplore.ieee.org.

Digital Object Identifier 10.1109/TGRS.2007.914804

temperature maps. This constraint also presents potential difficulties for the forward modeling of the scene brightness temperatures since this modeling is plagued by uncertainties and potential biases associated with rough sea surface scattering and emissivity models. Moreover, for the SMOS mission, the multidirectional nature of the measurements incorporated into the salinity retrieval at any given point on Earth results in a potentially wide range of celestial noise contamination for any given retrieval, so that failure to correct for the contamination prior to salinity retrieval may result in retrieved salinity errors and biases that are not easily correctable by further processing at a later stage.

The focus of this paper is given as follows: 1) to analyze the expected annual cycle of contamination of SMOS multiangular reconstructed brightness temperatures by scattered celestial radiation over the ocean and 2) to propose a method for the proper detection of and correct for this sky glitter within the SMOS ocean surface salinity retrieval algorithm.

For these two purposes, a sky brightness temperature map at L-band was generated for SMOS based on an existing all-sky continuum map using an approach similar to [2], and the method used to build this map is reviewed in Section II. Missing data in the vicinity of Cassiopeia A and other strong sources in the continuum map can potentially lead to underestimation of the reflected sky noise, particularly over smooth sea surfaces, and to address this issue, we derived an error map by using higher resolution surveys to identify the locations and brightness temperatures of sources that may introduce substantial errors associated with estimating the downwelling celestial radiation from the continuum map alone. Since these localized strong sources might require the use of very high-resolution grids when applying the modeling methodology developed in Part I, we evaluated the impact of resolution on the numerical scattering calculations and determined an acceptable discretization of the celestial noise map.

In Section III, we formulate expressions for the rough surface scattered celestial radiation incident at the SMOS antenna. The interferometric nature of the Microwave Imaging Radiometer by Aperture Synthesis (MIRAS) results in a formulation that is distinct from that for a real aperture radiometer. In developing these expressions, we consider, in turn, simplifications that are obtained by assuming that the sea surface is perfectly smooth and approximating the synthetic antenna weighting function by an isotropic function in director cosine (DC) coordinates.

Given the potential for scattered celestial noise to introduce seasonal and regional biases in retrieved surface salinity, we examined the seasonality and spatial distribution of the expected celestial sky glitter contamination for SMOS by performing a series of monthly orbit propagations in which we collected dwell lines, i.e., sets of multiangular scene brightness temperatures at a fixed location on Earth, over a fixed Earth grid that spans one complete orbit. The scattered celestial radiation was calculated for one orbit per month over a one-year period using idealized descriptions of the ocean surface state. Results of these calculations are presented in Section IV. The SMOS configuration, with its sun-synchronous orbit and large field of view (FOV), provides reconstructed brightness temperatures over a large range of incidence and azimuth angles (and therefore a large range of specular sky locations) at each point on Earth, so that a large portion of the sky will contribute to the contamination at any given time. Moreover, given the sun-synchronous nature of the SMOS orbit, the celestial sky glitter contamination is a function of time with a distinct annual cycle. This is distinct from the situation with the Aquarius/SAC-D mission, for which the set of all specular sky locations (or specular projection of the FOV) at any given time of year is a large closed loop on the celestial sphere. For SMOS, the error associated with assuming a perfectly smooth sea surface may exceed 0.1 K over large portions of the measurements in an orbit. Both the contamination and the potential error associated with assuming a perfectly flat surface are greatest for the descending passes from August to October.

Given the potential for significant impact of the rough ocean surface and the large computational burden associated with the scattering calculations, in Section V, we propose a practical correction and flagging strategy that may be used in a salinity retrieval algorithm. In Section VI, we summarize the results and briefly discuss potential sources of error as well as validation issues for the proposed celestial sky glitter correction.

II. Generation of an L-Band Sky Map to Be Used for SMOS Data Processing

Three components are required to build a map of the sky emission at L-band [2].

1) The cosmic microwave background (approximately a constant value of 2.725 K).
2) The neutral hydrogen line (HI in astronomer's shorthand): this strong emitting line is centered at 1420.4058 MHz and is spread over a finite band by an additional Doppler shift. In surveys of the continuum, this source is usually rejected by a stopband filter.
3) The continuum at $\sim$1.4 GHz, which originates from a variety of emission mechanisms (other lines than HI, synchrotron, free–free, thermal, blended emission of discrete radio sources,. . .).

The final merged map to be used with SMOS, which is termed here as the "nominal map," is expressed in the Besselian Epoch B1950 [4], and in what follows, we display the results (and perform the scattering calculations) in an equatorial coordinate system (with coordinates given by right ascension and declination) in this reference frame.

A. Main Sources of Data

To provide coverage of the whole sky, measurements obtained by different instruments situated in both the Northern and Southern Hemispheres must be combined. This requires extensive data collection and calibration to ensure sufficient data quality. The merging of these data sets requires cross calibration and consideration for differences in instrument angular resolutions. This work was conducted by experts in the field of radio astronomy, and the maps introduced here are based upon products produced by these experts.

1) Continuum: The data set identified here is a combination of the Northern Sky survey made with the Stockert radio

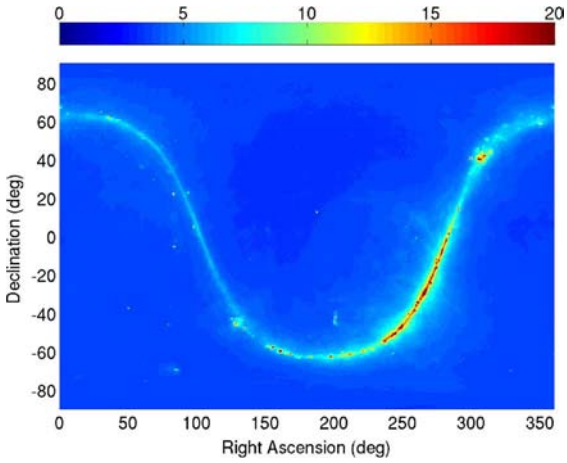

Fig. 1. Reich and Testori continuum map. Dark blue is for 0 K, and red is for 20 K.

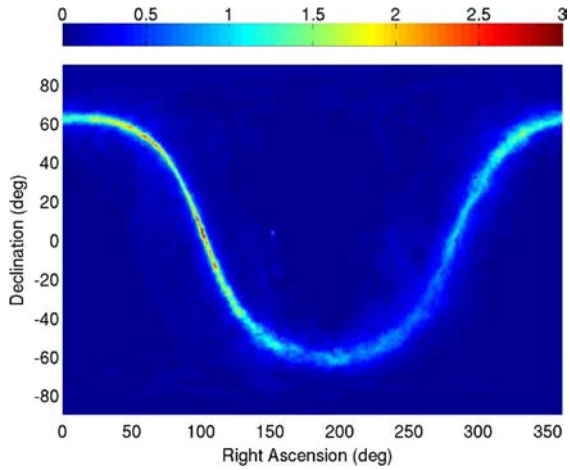

Fig. 2. HI map rescaled over SMOS bandwidth. Dark blue is for 0 K, and red is for 3 K.

telescope [5]–[7] and the Southern Sky survey made with the radio telescope of the Instituto Argentino de Radioastronomia (IAR) [8]. When the bandwidth of the receiver was overlapping the HI emission, a stopband filter centered over the HI line and 2 MHz wide was applied to the measurement to reject it. Data were sampled with a 0.25° resolution in both declination and right ascension (equatorial coordinates, B1950 system). The sensitivity (defined as three times the root-mean-square brightness temperature noise) of the merged data set is 0.05 K. In the following, this data set will be referred to as the Reich and Testori map (Fig. 1).

It is assumed that the "continuum" radiation, with unpolarized brightness temperature $T_{\rm cont}$, is broadband and therefore does not vary appreciably within the SMOS band. Thus, data from surveys made at slightly different center frequencies and with slightly different bandwidths may be directly combined. The continuum data set includes the constant 2.725 K cosmic background radiation.

2) Hydrogen Line: To account for the hydrogen line emission, we used the Leiden–Argentina–Bonn (LAB) survey [9]. The LAB survey contains the final data release of observations of 21-cm emission from galactic neutral hydrogen over the entire sky and is a merged product based on the Leiden–Dwingeloo survey of the sky north of $-30°$ [10] and the IAR survey of the sky south of $-25°$ [11], [12]. The source velocities away from the Earth range from -450 to $+400$ km $\cdot$ s^{-1} and are resolved in the data to 1.3 km $\cdot$ s^{-1}. The root-mean-square error of the brightness temperatures in the merged data set is 0.07–0.09 K (for each 1.3 km $\cdot$ s^{-1} layer). Data were sampled with a 0.5° resolution in both latitude and longitude (in galactic coordinates). Hereinafter, this data set will be referred to as the HI map.

3) Integration of HI Into the Continuum Map: As mentioned earlier, the continuum signal is broadband, with almost constant brightness temperature $T_{\rm cont}$ throughout the SMOS bandwidth. By contrast, the hydrogen line emission exists only over a very narrow band, but MIRAS measures radiation over a bandwidth $B_{\rm SMOS}$ of 19 MHz that includes the HI line (1420.4058 MHz) so that this narrow source must be integrated into the continuum map. The merged all-sky map provided by Reich and Testori includes both $T_{\rm cont}$ and the constant 2.725 K cosmic microwave background $T_{\rm CMB}$. The HI data [9] do not include $T_{\rm CMB}$ (Fig. 2).

To derive the HI line contribution over the SMOS bandwidth from HI line velocity range data, we used a Doppler relation between velocity range and frequency shift. The HI line frequency is $f_0 = 1420.4058$ MHz, and the Doppler shift is given by $f = f_0(c/(c+\nu))$, where c is the speed of light and ν is the relative speed of the source away from the Earth. The stopband filter applied to the Reich and Reich measurements is centered on f_0 and is $B_{\rm HI} = 2$ MHz wide. This corresponds to outward velocities ranging from -211.2 to $+211.4$ km $\cdot$ s^{-1}. Over this bandwidth, the contribution of HI signal is

$$\tilde{T}_{\rm HI} = \frac{1}{422.6 \text{ km} \cdot \text{s}^{-1}} \int_{-211.2 \text{ km}\cdot\text{s}^{-1}}^{211.4 \text{ km}\cdot\text{s}^{-1}} T_{\rm HI}(\nu) d\nu. \quad (1)$$

Finally, the resulting sky noise to be considered for SMOS is

$$T_{\rm sky} = T_{\rm CMB} + T_{\rm cont} + \tilde{T}_{\rm HI} \frac{B_{\rm HI}}{B_{\rm SMOS}}. \quad (2)$$

B. Gaps in the Continuum Survey: Use of Alternative Surveys and Source Catalogs for Missing Data Integration

The Reich and Testori continuum survey is not complete and contains regions with inadequate coverage. The most prominent such region is Cassiopeia A, where the high flux prevented accurate measurement using standard procedures. In addition, highly localized strong sources are not properly taken into account in the continuum survey. Higher resolution surveys that can alleviate this problem by providing auxiliary 1.4-GHz flux measurements for these problematic areas are available. These data sets usually come in two forms.

1) Higher resolution local sky maps where for a given area of the sky a radio flux is associated to each [right ascension, declination] cell. This enables an assessment of the slow variations of the background flux when it

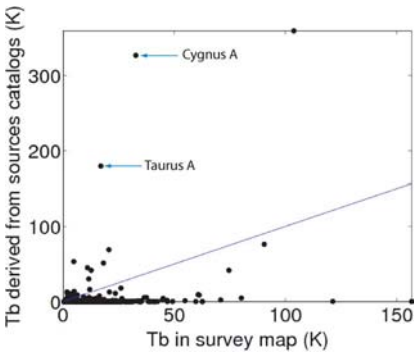

Fig. 3. Comparison between brightness temperatures derived from the individual source catalogs (NVSS + Parkes) and brightness temperatures extracted from the survey maps (i.e., a combination of the merged data from Reich and Testori, the rescaled HI line data from the survey in [9], and the Effelsberg survey data in the vicinity of Cassiopeia A). The diagonal line shows one-to-one correspondence.

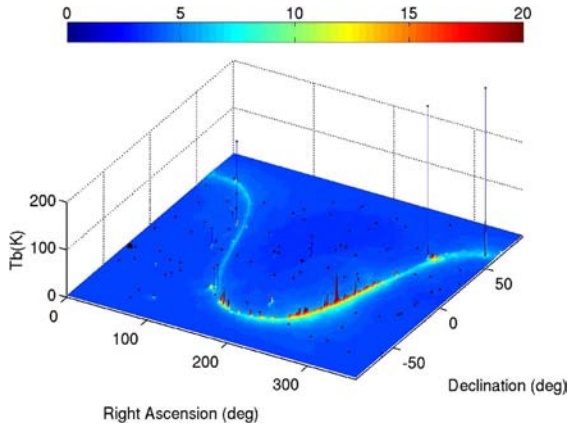

Fig. 4. Strong sources superimposed on the nominal SMOS sky map derived from the survey data of Reich and Testori, the rescaled HI line data from the survey in [9], and the Effelsberg survey data in the vicinity of Cassiopeia A. Only sources that exhibit a brightness temperature (for a 35-arcmin beam) larger than that in the nominal sky map are displayed.

results from the combination of minor sources that cannot be individually identified. Once rescaled and converted to the proper geometry, these data sets can be used to patch the continuum map where data are missing.

2) Source catalogs that provide flux measurements for specific strong sources with small angular extents. These data sets can be useful to identify strong sources in otherwise quiet areas of the sky.

In the case of strong sources of small angular extent, it is difficult to determine whether they are properly taken into account in the full sky survey map. To evaluate the extent to which strong sources are properly accounted for in the continuum map, a map of strong sources was generated from L-band source catalogs [13], [14], and we computed the corresponding brightness temperatures that would be collected by the Stockert/IAR radio telescopes (the ones that were used to generate the Reich and Testori map). These source data were obtained from both the [NRAO (National Radio Astronomy Observatory) VLA (Very Large Array) Sky Survey (NVSS)] [14] (Northern Hemisphere) and the Parkes [13] (Southern Hemisphere) catalogs. Only sources stronger than 0.3 Jy were considered, since smaller fluxes would introduce less than 0.015-K error in the Reich and Testori map.

The resulting brightness temperatures were compared with the combination of the continuum and HI maps. Fig. 3 shows that most sources exhibit a brightness temperature that does not exceed the corresponding continuum value (which is generally the case when the sources are embedded in regions of strong emission that dominate the total signal within the relatively large beam of the telescope). Nevertheless, some strong sources, such as Cygnus A and Taurus A, can be identified. Fig. 4 shows the locations of the sources for which the fluxes are underevaluated in the nominal sky map. Most discrepancies in the flux are quite small and are expected to be strongly reduced when integrated over the SMOS synthetic beam. The strongest discrepancies occur in the vicinity of Cygnus A and Cassiopeia A. The nominal sky map generated for SMOS was not corrected for these strong sources; instead, a separate sky map that contains only the strong source brightness temperatures averaged to the Stockert/Testori beamwidth was developed. As in [2], we do not account for possible polarization in either the nominal or the strong source maps.

C. Impact of Strong Sources

To quantify the maximum expected impact of strong point sources, we calculated the scattered signal along cross sections through Cassiopeia A, where the strongest sources are located, at both full $(0.25^\circ \times 0.25^\circ)$ and reduced-resolution $(3.75^\circ \times 3.75^\circ)$ celestial grid spacings for both the nominal and strong source maps. The reduced-resolution map was obtained by applying an energy flux-conserving averaging operator, which is described in the Appendix, to the full-resolution map. The results are shown in Fig. 5. To provide an indication of the spatial extent of the bistatic scattering cross sections on the celestial map, in Fig. 5(a), we overlay on the total celestial noise map (centered on Cassiopeia A) the weighting function associated with the scattering cross sections for a representative scattering calculation at a wind speed of 7 $\mathrm{m \cdot s^{-1}}$. The total scattered signal in the direction of the instrument is obtained by integrating the product of this weighting function and the sky brightness temperatures over the sky map. The downwind direction φ_w relative to the scattering azimuth ϕ_s (both defined to be positive counterclockwise from due east) is $\varphi_w - \phi_s = 0^\circ$. This weighting function has been normalized to a maximum of unity, and contours are shown at 0.1, 0.3, 0.5, 0.7, and 0.9. Clearly, the weighting function extends well beyond the localized strong source, so it is expected that the impact of such a source should be small. In Fig. 5(b), we show the scattered unpolarized signal $(1/2(T_v + T_h))$ along a cross section at constant declination in the celestial sphere, considering only the strong source map. In this cross section, the wind speed is fixed at 7 $\mathrm{m \cdot s^{-1}}$, the specular declination is 58.25°, the scattered field incidence angle is 0°, and the specular right ascension ranges from -40° to $+20^\circ$. The resulting glitter is shown for both the Kirchhoff approximation (KA) [15] and the first-order small slope approximation (SSA-1) [16] scattering models described in [3] and for both the full-resolution and reduced-resolution maps. The resulting glitter never exceeds

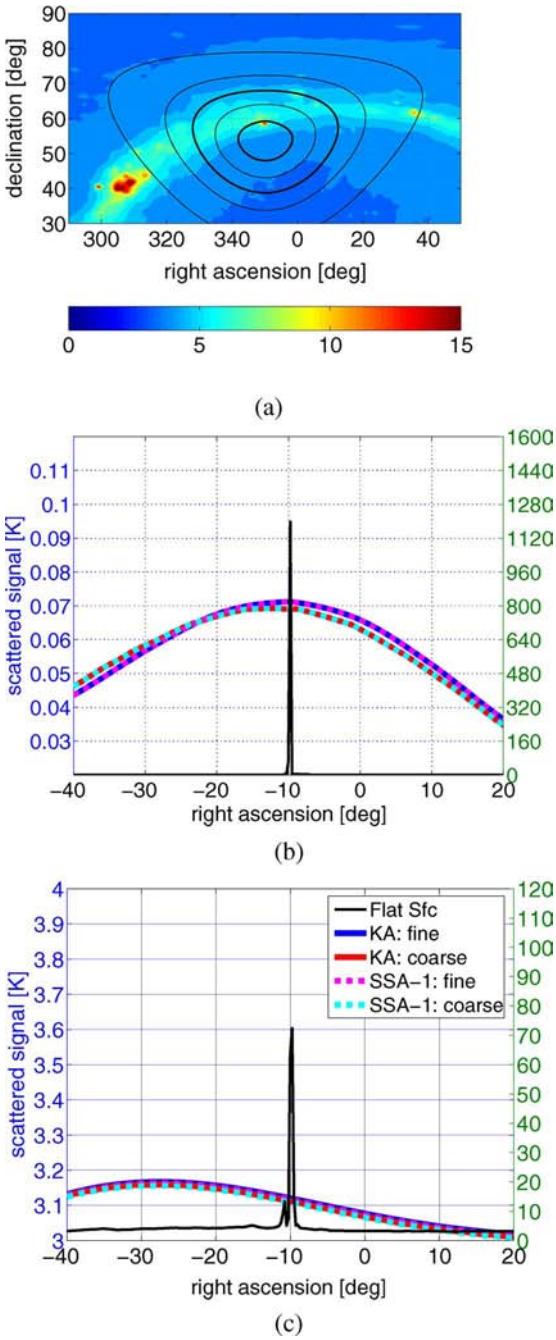

Fig. 5. (a) Incident unpolarized celestial noise. Overlaid is the bistatic scattering weighting function (discussed further in the text) for horizontal polarization for a specular point defined by $(\alpha_s = 350.25°, \delta_s = 58.5°)$ (Kirchhoff model; Kudryavtsev wave spectrum), which is normalized to unit amplitude. Thin contour lines correspond to the normalized levels (0.1, 0.3, 0.7), and thick contour lines correspond to the normalized levels (0.5, 0.9). (b) Cross section, at constant declination, of the unpolarized $(1/2(T_v + T_h))$ scattered radiation from strong sources as determined using the KA [15] and SSA-1 [16] electromagnetic models and the Kudryavtsev equilibrium ocean surface wave spectrum. Curves are defined in the inset of (c). The specularly reflected signal (solid black curve) is scaled to the right axis, whereas the scattered signals are scaled to the left axis. (c) Same as in (b) except for the nominal celestial noise map without strong sources. The scattered signal is evaluated at an incidence angle of $\theta_s = 0°$ and the incidence plane orientation angle $\psi_{uh} = 0°$. The surface wind speed is $u_{10} = 7\ \mathrm{m \cdot s^{-1}}$; the downwind direction relative to the scattering azimuth is $\varphi_w - \phi_s = 0°$. The maximum incident signal in the strong source map exceeds 1700 K, while in the nominal map the maximum signal in the vicinity of this strong source is approximately 150 K [with a maximum at a slightly displaced position of $(\alpha_s = 350.25°, \delta_s = 58.25°)$]. Units are in kelvin.

about 0.07 K, and the differences between solutions based on the two scattering models and two map resolutions are negligible, even for this source with a peak brightness temperature exceeding 1100 K.

Results from the same calculation with the nominal map are shown in Fig. 5(c), where it is seen that differences between resolutions and models are negligible, just as with the strong source map. Notably, the maximum in the glitter does not coincide with the strongest source, which can be understood by examination of Fig. 5(a), which shows that the maximum scattered signal can be expected when the overlap between the weighting function and the galactic equator reaches a maximum. This maximum occurs for a specular point displaced significantly from Cassiopeia A toward smaller right ascension.

III. Celestial Sky Glitter Contribution at the SMOS Instrument Level

In Part I, we examined the rough surface scattered noise without reference to a specific observational platform. Although the results of that study provide an indication of expected dependence of the scattered celestial sky glitter on both geophysical variables (such as wind speed and direction) and observational geometry, they do not address the impact of antenna patterns and the potential systematic contamination associated with orbit and viewing geometry. In this section, we consider the impact of the SMOS synthetic antenna weighting function on the resulting contamination.

A. General Formulation

Considering the simple case of unpolarized celestial radiation with scalar brightness temperature T_{sky} and assuming a simple exponential model for attenuation on both downward and upward paths, it was shown in Part I that the total antenna temperature Stokes component p (where p corresponds to either horizontal or vertical polarization) associated with rough sea scattered celestial radiation is

$$\overline{\mathbf{T}}_p^a = \frac{1}{\Omega_a} \int\limits_{\Omega_a} \frac{(\mathbf{G}\mathbf{M}_\alpha)}{4\pi\ \cos\ \theta_s} e^{-a\ \sec\ \theta_s} \times \int\limits_{\Omega_0(\Omega_a)} [\sigma_{pp}(\Omega_0) + \sigma_{pq}(\Omega_0)]\, e^{-a\ \sec\ \theta_0} T_{\mathrm{sky}}(\Omega_0) d\Omega_0 d\Omega_a \tag{3}$$

where the factor in front of the outermost integral normalizes the antenna gain pattern $\mathbf{G}$. As detailed in Part I, $\mathbf{M}_\alpha$ is a composite transformation matrix accounting for polarization basis and Faraday rotation. The scattered field incidence angle is θ_s, and σ_{pq} are the normalized bistatic scattering cross sections of the rough sea surface defined using the forward scattering alignment polarization basis convention as discussed in Part I and in [17]; Ω_a refers to the solid angle domain of integration over the antenna pattern and is associated with antenna incident and azimuth angles θ_a and ϕ_a, respectively; Ω_0 refers to the entire upper hemisphere of over which sky radiation is incident at the target; a is the zenith atmospheric

attenuation. Note that the normalized bistatic scattering cross sections used in this paper and in Part I differ from the bistatic scattering coefficients γ_{pq} used in [1] in that the normalized scattering cross sections relate scattered wave energy flux across the undisturbed scattering surface to the incident flux in the incident wave propagation direction, whereas the bistatic scattering coefficients relate the scattered energy flux across the surface to the incident energy flux across the surface, so that $\sigma_{pq} = \cos\,\theta_0 \gamma_{pq}$. This distinction is briefly discussed in [18].

In the case of an interferometric instrument such as MIRAS, we are concerned with modeling the reconstructed brightness temperature rather than the conventional antenna temperature as obtained from a real aperture radiometer. The reconstructed brightness temperature in direction (θ_a, ϕ_a) is still given by an equation of the form (3), but the outermost integral over Ω_a is evaluated over a rather narrow synthetic antenna weighting function centered at synthetic boresight direction (θ_a, ϕ_a), and the real aperture antenna gain matrix $\mathbf{G}$ is replaced by a synthetic antenna weighting function that, in general, depends upon both the instrument and the image reconstruction method. In what follows, we will use the terms "reconstructed brightness temperatures" and "brightness temperature measurements" interchangeably.

If we introduce instrument DC coordinates (ξ, η)

$$\xi = \sin\,\theta_a \cos\,\phi_a \tag{4}$$

$$\eta = \sin\,\theta_a \sin\,\phi_a \tag{5}$$

then the SMOS synthetic antenna weighting function, which is also called equivalent array factor (AF), may be written [19] as

$$\begin{aligned}\mathrm{AF}_{\mathrm{eq}}(\xi,\xi',\eta,\eta') = &\frac{\sqrt{3}}{2} d^2 \sum_m \sum_n W(u_{mn}, v_{mn}) \\ &\times \tilde{r}\left(-\frac{u_{mn}\cdot\xi + v_{mn}\cdot\eta}{f_0}\right) \\ &\times e^{j2\pi(u_{mn}\cdot(\xi-\xi')+v_{mn}\cdot(\eta-\eta'))}\end{aligned} \tag{6}$$

where W is the apodization function; $\tilde{r}$ is the fringe-washing factor (FWF), which accounts for the spatial decorrelation between antennas; u, v are the baseline coordinates in the frequency domain; d is the dimensionless antenna element spacing (0.875); f_0 is the central frequency (1413 MHz); ξ, η are the central (i.e., synthetic boresight) DC coordinates; and ξ', η' are the running DC coordinates. Defining $\mathcal{D} = \{\xi', \eta' : \xi'^2 + \eta'^2 < 1\}$ as the domain of integration within the synthetic beam and noting that

$$d\Omega_a = \sin\,\theta_a d\theta_a d\phi_a = \frac{d\xi\, d\eta}{\cos\,\theta_a} = \frac{d\xi\, d\eta}{\sqrt{1-\xi^2-\eta^2}} \tag{7}$$

the expression for the contribution of the polarized celestial sky glitter to the reconstructed brightness temperature in the Ludwig-3 polarization basis is given by

$$\begin{aligned}\overline{\mathbf{T}}_p^a(\xi,\eta) = &\iint_{\mathcal{D}} \frac{\mathrm{AF}_{\mathrm{eq}}(\xi,\xi',\eta,\eta')}{\sqrt{1-(\xi'-\xi)^2-(\eta'-\eta)^2}} \\ &\times \left[\mathbf{M}_\alpha(\xi',\eta')\mathbf{A}_u(\xi',\eta')\right] \tilde{\mathbf{T}}_p^a(\xi,\xi',\eta,\eta') d\xi' d\eta'\end{aligned} \tag{8}$$

where $\tilde{\mathbf{T}}_p^a(\xi,\xi',\eta,\eta')$ is the Stokes vector of the surface scattered celestial noise in the target polarization basis, and $\mathbf{A}_u$ is an upward atmospheric attenuation matrix defined in Part I. The variations in atmospheric attenuation and geometrical rotation are sufficiently small within the narrow (approximately 3°) synthetic beam that these factors may be approximated by their values at the synthetic beam center, i.e., (ξ, η), so that

$$\begin{aligned}\overline{\mathbf{T}}_p^a(\xi,\eta) \simeq &\mathbf{M}_\alpha(\xi,\eta)\mathbf{A}_u(\xi,\eta) \\ &\times \iint_{\mathcal{D}} \frac{\mathrm{AF}_{\mathrm{eq}}(\xi,\xi',\eta,\eta')}{\sqrt{1-(\xi'-\xi)^2-(\eta'-\eta)^2}} \tilde{\mathbf{T}}_p^a(\xi,\xi',\eta,\eta') d\xi' d\eta'.\end{aligned} \tag{9}$$

As shown in [20], if one neglects the FWF, the AF may be approximated by a rather narrow centrosymmetric function that is independent of the location of the synthetic boresight (ξ, η) within the FOV. The following explicit formula has been developed to approximate the actual AF with no FWF effect:

$$\begin{aligned}\mathrm{AF}_{\mathrm{eq}}(\xi,\xi',\eta,\eta') &\simeq F_{\mathrm{cs}}\left(\rho(\xi,\xi',\eta,\eta')\right) \\ &= \max\left\{0, \left[\frac{\sin\, k_f\cdot\rho}{k_f\cdot\rho}\right]^{k_k} \cdot \frac{1}{1+k_g\cdot\rho^{k_h}}\right\}\end{aligned} \tag{10}$$

where $\rho = \sqrt{(\xi'-\xi)^2+(\eta'-\eta)^2}$ is the distance in DC coordinates, $k_f = 73.30$, $k_g = 524.5$, $k_h = 2.1030$, and $k_k = 1.4936$. Throughout the rest of this paper, we refer to the approximate AF expression (10) as the antenna weighting function, i.e., WEF. If we adopt this approximate formulation for the AF and assume that the downwelling sky radiation is unpolarized, then the total contamination of reconstructed brightness temperatures by scattered celestial sky glitter (3) becomes

$$\begin{aligned}\overline{\mathbf{T}}_p^a(\xi,\eta) \simeq &\frac{\mathbf{M}_\alpha(\xi,\eta)}{4\pi\,\cos\,\theta_s(\xi,\eta)} e^{-a\,\sec\,\theta_s(\xi,\eta)} \iint_{\mathcal{D}_\rho} d\phi\, d\rho \frac{\rho F_{\mathrm{cs}}(\rho)}{\sqrt{1-\rho^2}} \\ &\times \int_{\Omega_0} \left[\sigma_{pp}(\Omega_0) + \sigma_{pq}(\Omega_0)\right] e^{-a\,\sec\,\theta_0} T_{\mathrm{sky}}(\Omega_0) d\Omega_0.\end{aligned} \tag{11}$$

In this equation, $\mathcal{D}_\rho = \{\rho, \phi : (\xi'(\rho,\phi))^2 + \eta'((\rho,\phi))^2 < 1\}$ is the polar coordinate domain corresponding to the Cartesian domain $\mathcal{D}$.

B. Perfectly Smooth (Flat) Sea Surface Case

When the sea surface is perfectly flat, the scattered celestial sky glitter incident at the instrument in the surface polarization basis reduces to

$$\tilde{\mathbf{T}}_p^f = \left|R_{pp}^{(0)}(S, T_s, \theta_s)\right|^2 T_{\mathrm{sky}}(\theta_s, \phi_s - \pi) e^{-a\,\sec\,\theta_s} \tag{12}$$

where $R_{pp}^{(0)}(S, T_s, \theta_s)$ are the Fresnel reflection coefficients of the flat sea surface with salinity S, physical surface temperature T_s, incidence angle θ_s, and linear polarization p. In this case,

the contribution to the reconstructed brightness temperature from the sky glitter incident at the antenna from direction (ξ, η), which is expressed in the instrument polarization basis, is

$$\overline{T}_p^{\mathrm{fa}}(\xi,\eta) \simeq (\mathbf{M}_\alpha(\xi,\eta)\mathbf{A}_u(\xi,\eta)) \iint_{\mathcal{D}} \frac{\mathrm{AF}_{\mathrm{eq}}(\xi,\xi',\eta,\eta')}{\sqrt{1-(\xi'-\xi)^2-(\eta'-\eta)^2}} \times \left| R_{pp}^{(0)}\left(S, T_s, \theta_s(\xi',\eta')\right)\right|^2 \times T_{\mathrm{sky}}(\xi,\eta,\xi',\eta') e^{-a\sec\theta_0(\xi',\eta')} d\xi' d\eta'. \quad (13)$$

The Fresnel power reflection coefficients vary weakly over the significant portion of the synthetic beam, so that

$$\left| R_{pp}^{(0)}\left(S, T_s, \theta_s(\xi',\eta')\right)\right|^2 \simeq \left| R_{pp}^{(0)}\left(S, T_s, \theta_s(\xi,\eta)\right)\right|^2. \quad (14)$$

With this approximation, the celestial sky glitter contribution at the SMOS antenna for a perfectly flat sea surface becomes

$$\overline{T}_p^{fa}(\xi,\eta) \simeq \mathbf{M}_\alpha(\xi,\eta) e^{-a\ \sec\ \theta_s(\xi,\eta)} \left| R_{pp}^{(0)}\left(S, T_s, \theta_s(\xi,\eta)\right)\right|^2 \times \iint_{\mathcal{D}_\rho} \frac{\rho F_{\mathrm{cs}}(\rho)}{\sqrt{1-\rho^2}} T_{\mathrm{sky}}(\xi,\eta,\rho,\phi) e^{-a\ \sec\ \theta_0(\phi,\rho)} d\phi\, d\rho. \quad (15)$$

If we ignore the downward atmospheric attenuation, then the approximate formulation (15) for a perfectly smooth ocean surface is particularly attractive from a processing point of view because it allows the incorporation of the antenna pattern effect by a presmoothing of the sky brightness temperature map [i.e., the integral factor in (15)] with the idealized synthetic antenna weighting function. The synthetic beam-weighted reflected celestial sky glitter contamination may then be obtained for arbitrary viewing geometry with a simple interpolation from the smoothed map followed by a matrix multiplication.

C. Antenna Pattern Smoothing Versus Roughness Spreading

Following (11), to properly account for the celestial glitter in the presence of surface roughness, we must compute the scattered noise throughout the synthetic beam and then integrate the product of the weighting function F_{cs} and this scattered signal. Such a computation is not practical, and hence, it is useful to determine if we can avoid this averaging operation. To assess the impact of the synthetic beam averaging, we selected a time and satellite configuration such that a small but strong brightness source exists inside the SMOS FOV. We then established a fine mesh over a small portion of the FOV surrounding this source (a 65 × 65 regular grid covering a 0.2 × 0.2 domain in the antenna DC coordinates) and calculated the scattered horizontally polarized signal (in the surface polarization basis) at each grid point. The flat surface reflected signal with no synthetic beam smoothing, which is shown in Fig. 6(a), exhibits a maximum brightness temperature of approximately 50 K. The corresponding signal as smoothed by the synthetic beam, which is shown in Fig. 6(b), is significantly smoother, with a maximum brightness temperature of approximately 16 K.

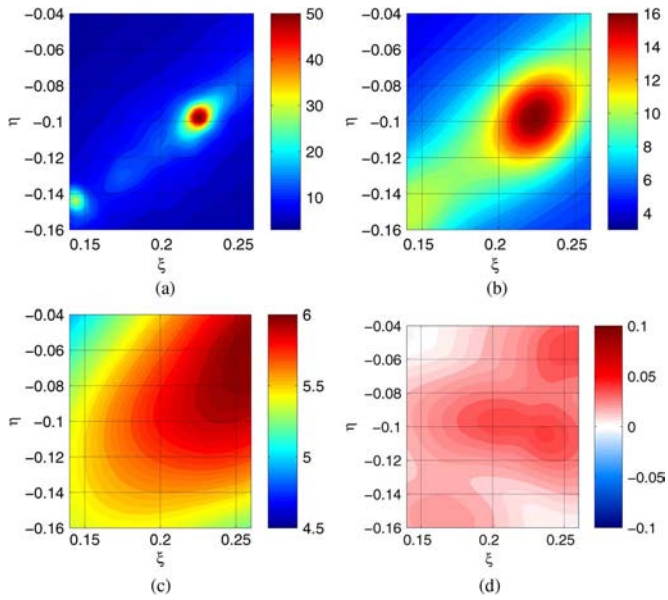

Fig. 6. (a) Flat sea surface specularly reflected signal at horizontal polarization. (b) Flat sea surface specularly reflected signal at horizontal polarization weighted by centrosymmetric WEF. (c) Bistatically scattered signal at horizontal polarization for a wind speed of 3 m/s. (d) Difference between scattered horizontally polarized celestial noise with and without weighting by the WEF. Units are in kelvin.

However, based on the scattering solutions obtained in this paper, the impact of synthetic beam smoothing is far less than that owing to the directional spreading of the radiation by the roughened ocean surface, even at a wind speed of 3 $\mathrm{m \cdot s^{-1}}$ [Fig. 6(c)]. This rough surface smoothing is sufficiently large that applying the WEF smoothing to the scattering solutions yields little change (generally less than about 0.05 K), as shown in Fig. 6(d). We conclude that the application of the WEF is not necessary in the presence of surface roughness, so long as this roughness is uniform within the synthetic antenna beam. Although the WEF impact might be nonnegligible for surface roughness at wind speeds lower than 3 $\mathrm{m \cdot s^{-1}}$ or for highly heterogeneous rough surfaces, in what follows, we neglect this impact except for perfectly smooth surface conditions.

Without the WEF smoothing, the contribution of rough surface scattered celestial sky glitter to the reconstructed brightness temperatures reduces to

$$\overline{\mathbf{T}}_p^a(\xi,\eta) \simeq \frac{\mathbf{M}_\alpha(\xi,\eta)}{4\pi\ \cos\ \theta_s(\xi,\eta)} e^{-a\ \sec\ \theta_s(\xi,\eta)} \times \int_{\Omega_0} \left[\sigma_{pp}(\Omega_0) + \sigma_{pq}(\Omega_0)\right] e^{-a\ \sec\ \theta_0} T_{\mathrm{sky}}(\Omega_0) d\Omega_0 \quad (16)$$

and this equation is the basis for the results that follow.

IV. Annual Cycle of Celestial Sky Glitter Contamination for SMOS

A. Orbit Propagation and Dwell Line Generation

Having established a reasonable approximation for the impact of scattered celestial noise on the measurements, we now quantify the impact of celestial sky glitter on SMOS

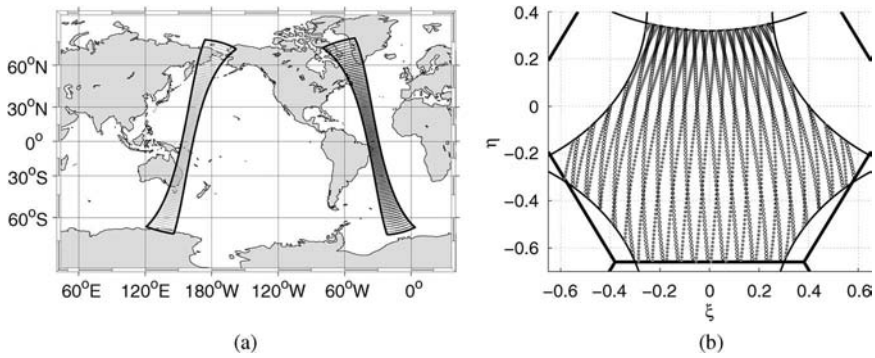

Fig. 7. (a) Fixed points on Earth at which we compute dwell lines for both ascending and descending swaths. (b) Projections of dwell lines in DC coordinates. Circles correspond to an ascending pass, while solid dots correspond to a descending pass.

measurements throughout the year. Given the sun-synchronous nature of the SMOS orbit, the sky noise impact is expected to exhibit a distinct annual cycle. To examine this annual cycle, we performed a series of orbit propagations, with successive orbits spaced roughly one month apart. Although we considered both idealized and realistic geophysical conditions, here, we present only the results from the idealized simulations (with constant roughness conditions) to emphasize the impact of the viewing geometry on the results. Introducing spatial and temporal variabilities in the surface wind speed complicates the interpretation of statistics and obscures the results, and the expected behavior in variable wind conditions may be anticipated from the results presented in Part I. For the present simulations, bistatic scattering cross sections were evaluated at a constant SSS of 35 psu and temperature of 15 °C. As discussed in Part I, these two geophysical parameters will have a small impact on diffuse scattering of celestial sky radiation. For comparison purposes, these surface conditions were also used to estimate the contamination assuming a perfectly smooth ocean surface. Moreover, to simplify the interpretation, we neglected downward and upward atmospheric attenuation and only considered results for the first Stokes parameter (which is not affected by the Faraday rotation on the upward path across the ionosphere).

Orbit simulations were conducted using the same orbital and instrument configuration anticipated for the actual satellite. SMOS will be placed in a circular sun-synchronous low Earth orbit at a mean flight altitude of 755 km. The local time of the ascending node will be 6:00 A.M., and the inclination of the orbital plane will be 98.42°. In addition, the antenna array plane will be tilted from the horizontal by 32°. To produce one orbit simulation, we first established a fixed Earth grid by propagating the satellite through one orbit at a time step of 24 s and projecting onto the Earth's surface a set of points along a cross-track line at $\eta = 0.0$ in the instrument frame DC coordinates. As illustrated in Fig. 7(a), this procedure establishes a 21×250 point fixed grid $\mathbf{E}_{ij}$ on the Earth's surface, with 250 rows (with index i) of 21 projected $\eta = 0$ points (with index j). Having established this grid, we then propagated the satellite through the same orbit but with a 2.4-s time step, producing a set of snapshots $\mathcal{S}_k$. At each of the 21×250 grid points in a given SMOS FOV, we recorded parameters such as the incidence and azimuth angles at target and the location in antenna frame (ξ_s, η_s). The result is a grid of dwell lines, where a dwell line at grid point (i, j), which is denoted as $\mathcal{D}_{ij}$, consists of a set of all k for which $\mathcal{S}_k$ contains the point $\mathbf{E}_{ij}$ together with the corresponding set of positions in those snapshots, i.e.,

$$\mathcal{D}_{ij} = \{k, \xi(i,j,k), \eta(i,j,k) : (\xi(i,j,k), \eta(i,j,k)) \in \mathcal{S}_k\}. \tag{17}$$

Fig. 7(b) shows examples of dwell lines in DC coordinates.

In the following experiments, we configured each orbit in the monthly sequence of orbits so that the grid points do not change location from one month to the next. Since we only consider constant geophysical conditions, this has no significance beyond the fact that the geographical locations of the grid points remain the same from one month to the next.

B. Perfectly Smooth Sea Surface Contamination

Before evaluating the impact of rough surface scattered sky noise, we establish the impact of flat surface reflected noise as a baseline. In Fig. 8, we show for each orbit the fraction of measurements contaminated by unpolarized reflected celestial noise $(1/2(T_v + T_h))$ exceeding 4 K. Most notable is the fact that the reflected celestial sky noise is quite different for the ascending and descending swaths, with generally larger contamination in the descending swaths, which is to be expected since the specular points for dwell lines on the descending swaths tend to be aligned with the strongest portion of the noise originating near the galactic equator. The contamination is greatest during the northern hemisphere autumn when the specular points tend to be nearest the galactic equator. A significant portion of the dwell lines for the September 28 descending swath have nearly 90% of their reconstructed brightness temperatures contaminated by flat surface reflected noise exceeding 4 K. The viewing geometry along any given dwell line is such that the contamination patterns tend to be elongated in the FOV. There is no time of the year that the entire swath is severely contaminated. However, during certain times of the year, the fraction of measurements suffering significant contamination may be large. The contamination is also a function of latitude, and the descending swaths in September tend to suffer from more contamination in the Northern Hemisphere than in the

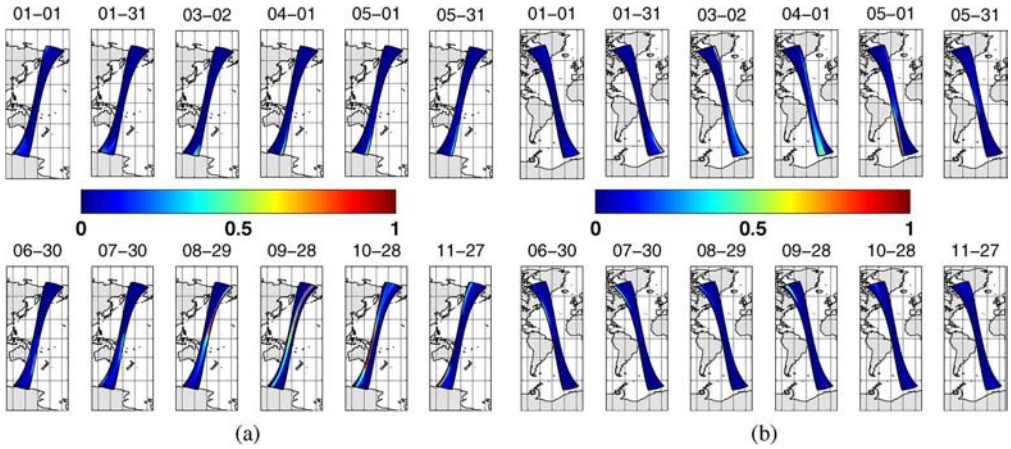

Fig. 8. Fraction of dwell line brightness temperature measurements contaminated by perfectly smooth sea surface reflected celestial noise $(1/2(T_v + T_h))$ greater than 4 K, for each month of the year. (a) Descending swaths. (b) Ascending swaths. The orbit dates (month–day) are indicated above each swath.

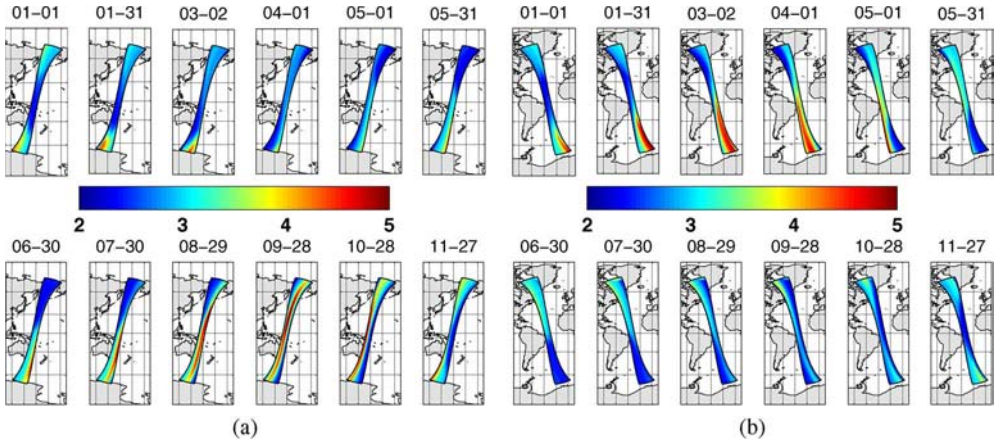

Fig. 9. Maximum unpolarized scattered celestial noise $(1/2(T_v + T_h))$ over all measurements of each dwell line for (a) descending and (b) ascending swaths. The wind speed is 7 m $\cdot$ s^{-1}, and the downwind direction is 0°. The Kudryavtsev wave spectrum and the KA scattering model are used to compute the scattered signal. Solutions are expressed in kelvin.

Southern Hemisphere. In October, the contamination maximum shifts to the Southern Hemisphere.

C. Rough Surface Contamination

Although examination of the flat surface reflected celestial noise provides some indication of expected contamination patterns, it does not provide a realistic picture of the true magnitude of the contamination, since at any given time only about 5% of the Earth's ocean surface is nearly perfectly smooth [21]. As discussed in Part I, the differences between the smooth surface reflected and rough surface scattered signals may be large, even at wind speeds below 7 m $\cdot$ s^{-1}. In this section, we examine the expected contamination pattern for SMOS in idealized rough sea surface conditions with a constant wind speed of 7 m $\cdot$ s^{-1} and downwind direction of 0°. Using the Kudryavtsev equilibrium wave spectrum [22] and the Kirchhoff scattering model (see Part I), we computed the expected rough surface scattered celestial noise over the same dwell lines considered in the previous section. In Fig. 9, we show the maximum predicted unpolarized scattered sky noise $(1/2(T_v + T_h))$ for both descending and ascending passes throughout the year. Both the spatial and temporal structures of the contamination are similar to those of the flat surface contamination, but in the rough surface case, the patterns tend to be smoother with significantly lower maximum contamination, as one would expect from the results presented in Part I. The strong maximum contamination first appears in late June in the southern hemisphere and propagates across the FOV toward higher ξ in DC coordinates as time progresses. By September 28, the peak contamination is situated near the middle of the swath and nearly extends from pole to pole on Earth. By late November, this maximum has shifted off the right-hand side of the FOV.

In the ascending swaths, the time of year of maximum contamination is different. The peak contamination, which is slightly smaller in magnitude (approximately 4.7 K) than for the descending swaths, begins to enter the swath in early January and propagates toward the west and north within the swath, reaching the domain center in March, when it extends from the South Pole to near the Earth's equator. By the end of May, the peak has nearly left the swath.

The results for all of the orbits show that the time periods of maximum contamination for the ascending and descending swaths are nearly disjoint. At any given time of the year, either the ascending or descending swaths, but not both, will suffer

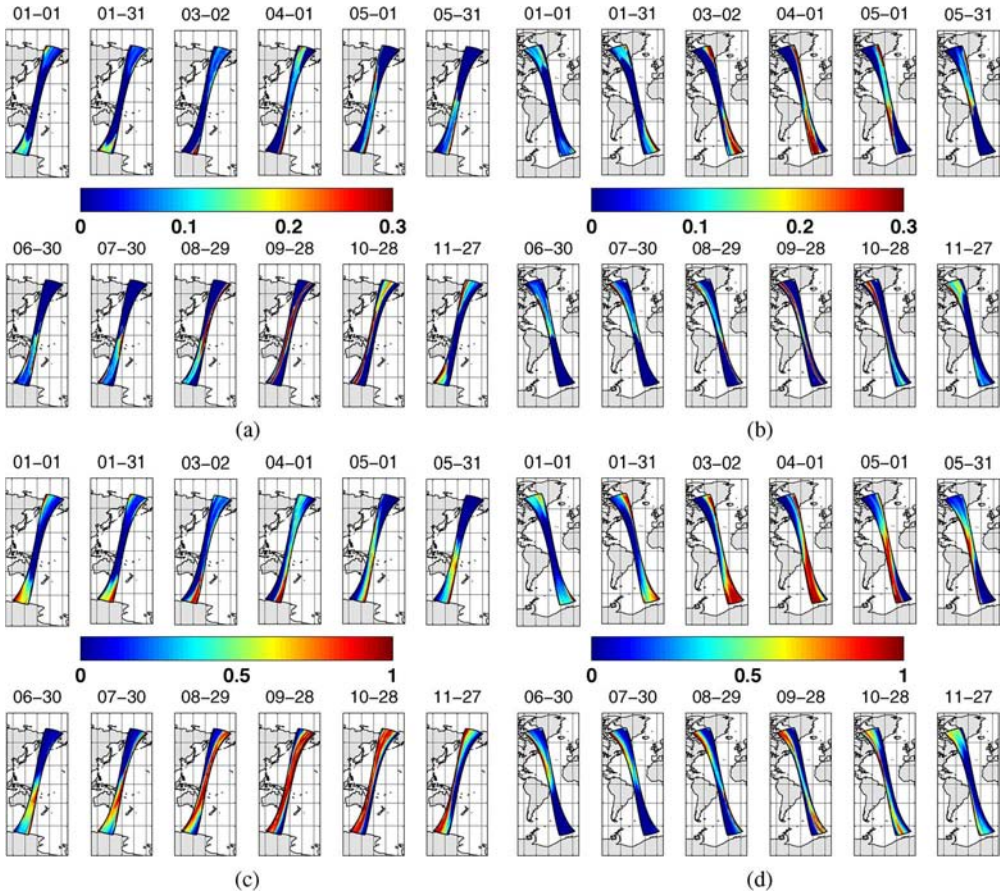

Fig. 10. (a) and (b) Fraction of dwell line brightness temperature measurements for which the difference between the unpolarized flat surface reflected signal $(1/2(T_v + T_h))$ differs from the bistatically scattered signal by more than 0.5 K, for descending and ascending swaths, respectively; (c) and (d): Same as in (a) and (b) except that the cutoff difference is 0.1 K. The geophysical conditions are the same as in Fig. 9.

contamination. Given the relative ease with which contamination of reconstructed brightness temperatures by flat surface reflected celestial noise may be evaluated, it is important to determine if a more involved computation of the rough surface scattered celestial noise will yield significantly different results. Therefore, we assessed the overall difference between results based on flat surface reflection and those based on rough surface scattering calculations. Fig. 10(a) shows, at each dwell line of the descending swaths, the fraction of measurements for which the absolute difference between the perfectly smooth and rough surface solutions exceeds 0.5 K. The maxima in this fraction generally exceed 10% and tend to coincide with the maxima in the contamination. Similar results were obtained for the ascending swaths [Fig. 10(b)]. The fraction of measurements for which the difference between the flat and rough solutions exceeds 0.1 K approaches 100% for a substantial number of dwell lines, as shown in Fig. 10(c) and (d). Given that the maxima in the difference between the flat and rough surface solutions tend to coincide with the maxima in the flat surface reflected noise, one might hope to be able to develop a correction and error flagging strategy based upon the flat surface solution. Unfortunately, the differences between the flat and rough surface solutions do not exactly coincide with the flat surface solution because the rough surface scattering solutions depend strongly upon the spatial structure of the source in the vicinity of the specular direction; therefore, it is not possible to determine a universal threshold based on the flat surface solution alone.

V. Processing Issues

Given the significant and systematic impact of ocean surface roughness on the contamination of reconstructed brightness temperatures by celestial sky glitter, it is certainly desirable to have a practical correction and flagging strategy for operation purposes that incorporates the effect of surface roughness. Unfortunately, it is not practical to perform per-measurement integrations of (16) to obtain scattering solutions, particularly given the proposed SMOS level 2 iterative SSS inversion scheme in which the surface wind speed is adjusted until convergence to a solution for the salinity is achieved. The proposed solution for SMOS level 2 processing involves precomputing the scattered celestial noise for a range of wind speeds, incidence angles, specular sky locations, and the incidence plane orientation angle ψ_{uh} introduced in Part I. The precomputed results are stored in a lookup table from which solutions are obtained during the salinity inversion procedure by interpolation. The change of variables introduced in Part I involving the incidence plane orientation angle ψ_{uh} allows the separation of the impact of viewing geometry at the target from the impact of specular sky location, thereby enabling the creation of a lookup table

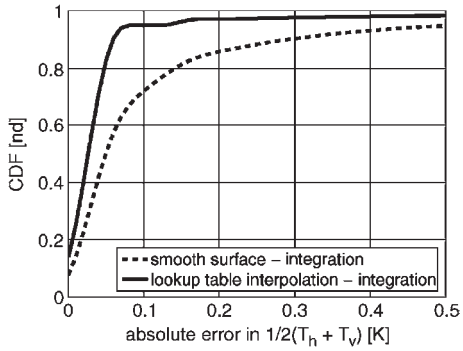

Fig. 11. Cumulative distribution function of the difference between $(1/2(T_h + T_v))$ obtained by interpolation from the lookup table and by the per-measurement computation of the scattering solutions (solid curve). Cumulative distribution function of the difference between $(1/2(T_h + T_v))$ obtained by use of the weighted flat surface reflection model and by the per-measurement computation of the scattering solutions (dashed curve). The differences are shown for the April ascending orbit only, and the geophysical conditions are the same as in Fig. 10. The Kudryavtsev wave spectrum and the KA electromagnetic scattering model are used for both the lookup table generation and the per-measurement integrations.

with practical discretizations in all dimensions. For the results presented in this paper, we have generated scattered celestial noise solutions for wind speeds of 3, 5, 7, 10, 15, and 25 m $\cdot$ s^{-1} on a regular $3.75^\circ \times 3.75^\circ$ grid in specular right ascension and declination. The grid spacing in ψ_{uh} is 22.5°, and the incidence angles range from 0° to 60° by 5° and from 60° to 80° by 10°. To evaluate the performance of this lookup table solution, we considered the same uniform geophysical conditions as in the previous section and computed, for each measurement of each dwell line, the difference between the solution obtained from numerical integration of (16) and that obtained from multilinear interpolation from the lookup table. The solid curve in Fig. 11 shows the cumulative distribution function of the absolute difference between these two computation methods for ascending swath on April 1, when we expect the worst contamination for ascending passes. The absolute difference in the unpolarized signal $(1/2(T_v + T_h))$ is less than 0.1 K in about 95% of measurements, which is far better than that obtained with the perfectly smooth surface solution. For comparison, the dashed curve in the same figure shows the cumulative distribution function of the difference between the WEF-weighted flat surface reflection model and the per-measurement integration results. Similar results were found for the September 28 descending swath. Therefore, the lookup table approach represents the per-measurement integration with sufficient fidelity that it is appropriate for use in an operation processor. Moreover, the approach easily accommodates alternative scattering models. The strong directional spreading effect of the rough ocean surface permits the creation of the lookup table by integration over a reduced resolution sky map with a grid spacing of $3.75^\circ \times 3.75^\circ$ in right ascension and declination. Presently, the rough surface scattering solutions are implemented for wind speeds greater than 3 m $\cdot$ s^{-1}. At zero wind speed, the WEF-weighted smooth surface solution given in (15) is implemented using the nominal high-resolution sky map (with $0.25^\circ \times 0.25^\circ$ grid spacing and strong sources excluded). For nonzero wind speeds below 3 m $\cdot$ s^{-1}, surface roughness spectral descriptions are known to be inaccurate, and the approach we take to estimate the celestial sky glitter contamination in this low wind speed range is to linearly interpolate between solutions for the perfectly smooth and 3 m $\cdot$ s^{-1} rough surfaces. Although this approach lacks physical basis, it is proposed here as a practical solution in the absence of an adequate rough surface statistical description for low surface wind speeds. It is anticipated that the algorithm will be refined based on SMOS data obtained after launch.

VI. Summary and Discussion

In this paper, we have examined how the rough sea surface scattering of L-band celestial sky radiation might affect SMOS measurements.

We began by presenting the nominal celestial sky brightness temperature map at L-band that was generated for SMOS using an approach similar to that described in [2]. The nominal map includes the appropriately integrated impact of the hydrogen line emission, but the impact of highly localized strong sources is neglected. Since omission of these strong sources from this nominal sky map may introduce errors into the scattering calculations, we also derived a map of strong sources and their brightness temperatures using high-resolution surveys. We found that, for wind speeds greater 3 m $\cdot$ s^{-1} and for the two rough surface scattering models (KA and SSA-1) considered in this paper, the scattered signals associated with these localized strong sources are extremely small owing to the directional spreading of the scattered signal by the rough surface. Therefore, in the scattering calculations, we neglected the impact of such sources.

Next, we established expressions for the expected signals at the SMOS antenna array for both flat (perfectly smooth) and rough seas. Using an approximate isotropic (in DC coordinates) synthetic antenna weighting function (i.e., WEF), we obtained expressions for the contribution of the scattered celestial sky radiation to the total reconstructed brightness temperatures. In theory, to properly assess the impact of celestial glitter in the presence of surface roughness on the reconstructed brightness temperatures, the scattered noise must be computed over the instrument FOV and then integrated over the synthetic antenna weighting function. Given the extreme computational burden of this approach, we evaluated the impact of computing only the synthetic boresight solution and avoiding the WEF integration entirely. We found that, in general, the rough surface scattered signal is sufficiently smooth that, even in the vicinity of a strong (i.e., 50 K) localized source, the scattered signal is not modified by more than approximately 0.05 K by integration over the WEF, so that this step may be avoided in rough ocean surface conditions. Although the WEF impact might be nonnegligible for surface roughness at wind speeds lower than 3 m $\cdot$ s^{-1} or highly heterogeneous rough surfaces, we do not consider it, except for the perfectly smooth surface conditions.

The sampling characteristics of the instrument are important factors in determining the overall impact of scattered celestial noise for a particular mission. Both the Aquarius/SAC-D and SMOS satellites will maintain sun-synchronous orbits, so that the specular reflection of the antenna pattern on the celestial

sphere will slowly evolve with time, making one complete cycle in a year. As compared with Aquarius/SAC-D, the large FOV of MIRAS is associated with a much larger specular domain in the celestial sphere, thus the reconstructed brightness temperatures derived from MIRAS will suffer from a large range of contamination at any given dwell line on Earth. The results presented here indicate that the contamination exhibits a strong seasonal cycle that is different for the ascending and descending swaths. The largest contamination occurs in the descending swath in September and October, when the specular projection of the FOV is aligned with a strip of strong noise in the vicinity of the galactic equator. The geometry of the problem is such that contamination patterns tend to be elongated in the along-track direction. Moreover, during one period of time each year, the specular projections of dwell lines for both the ascending and descending swaths will be aligned with the galactic equator, and during this time period, contamination will be most severe. Considering the flat sea surface reflected signal alone, a significant fraction of the measurements in many of the dwell lines will be contaminated by reflected celestial noise exceeding 4 K in the descending swath during September and October (and to a large extent in August and November). Considering moderate wind speed conditions, a larger portion of dwell lines will suffer from contamination in which surface roughness modifies the flat surface specularly reflected signal by more than 0.1 K.

Given this potential for strong contamination in a large fraction of measurements and the computational burden of the rough surface scattering calculations, we examined a strategy for computing the rough surface scattered signal using a precomputed lookup table expressed in terms of the specular sky location, incidence angle, wind speed, and the incidence plane orientation angle ψ_{uh} introduced in Part I. For the monthly orbits considered here, results obtained by interpolation from the lookup table differ from per-measurement scattering calculations by less than 0.1 K in 95% of measurements for April and September, during which we expect the worst contamination and the largest impact of surface roughness.

In the monthly orbit calculations with a moderate surface wind speed, only 70% of the rough surface scattered signals differ from the smooth surface counterparts by less than 0.1 K. Importantly, the numerically integrated scattered signals are based on asymptotic scattering models, and the statistical description of the rough surface is based on an idealized wave model. Although we found that in the vicinity of the strongest noise source the results obtained from two electromagnetic models do not differ by more than 0.02 K, the amplitudes and phases of the wind direction dependence can exhibit large differences between models. In addition, we have not considered here the dependence of the results on the wave model, which may have a significant impact on the contamination and its relative wind direction dependence.

Finally, we have not considered polarized source radiation. Recently, new surveys of linearly polarized radiation (i.e., the third and fourth Stokes parameters) over the northern sky at a frequency of 1.4 GHz have become available [23]–[26]. These maps reveal a highly variable polarized intensity that can reach 500 mK in magnitude (e.g., in the vicinity of the North Polar Spur). This polarization, which is neglected in our formulation, might impact the celestial noise contamination to an extent that is significant for SSS retrieval. Unfortunately, incorporation of this polarization complicates the formulation. In particular, the polarimetric algorithm must account for polarization rotation from the celestial basis to the usual target basis as well as downward Faraday rotation. Generalizing the expression for the total scattered brightness temperature in the antenna frame (3) to the fully polarized case, we obtain

$$\overline{\mathbf{T}}_p^a = \frac{1}{\Omega_a}\int\limits_{\Omega_a} \frac{(\mathbf{G}\mathbf{M}_\alpha)}{4\pi\,\cos\theta_s} e^{-a\,\sec\theta_s} \times \int\limits_{\Omega_0(\Omega_a)} \mathbf{M}_s(\Omega_a,\Omega_0)\mathbf{M}_{\mathrm{fd}}(\Omega_0,t)\mathbf{M}_\Psi \mathbf{T}_q e^{-a\,\sec\theta_0} d\Omega_0 d\Omega_a \tag{18}$$

where $\mathbf{T}_q = (\mathbf{T}_h, \mathbf{T}_v, \mathbf{U}, \mathbf{V})^T$ is the full Stokes vector of incidence radiation, and $\overline{\mathbf{T}}_p^a$ is the Stokes vector of the WEF-weighted signal in the instrument polarization basis. In contrast with the formulation given in [3], which is appropriate for unpolarized sky radiation, $\mathbf{M}_s(\Omega_a,\Omega_0)$ is the fully polarimetric Mueller matrix (with the obvious dependence on the rough surface omitted). The incoming Stokes vector $\mathbf{T}_q$ is transformed before scattering by a change in polarization basis $\mathbf{M}_\Psi(\Omega_0)$ and the time-dependent Faraday rotation $\mathbf{M}_{\mathrm{fd}}(\Omega_0,t)$, which in turn depends upon the incident radiation direction. The transformation matrix $\mathbf{M}_\Psi(\Omega_0)$ implicitly depends on the target location and radiometer incidence and azimuth angles, but these additional dependencies may be accounted for by the incidence plane orientation angle ψ_{uh} introduced in Part I, so that more explicitly $\mathbf{M}_\Psi = \mathbf{M}_\Psi(\psi_{uh},\Omega_0)$. Therefore, without Faraday rotation, no additional difficulties are encountered in the formulation of the lookup table. When we perform the integration of the fully polarimetric scattering cross sections over the upper hemisphere for each $\{\alpha_s,\delta_s,\theta_s,\psi_{uh}\}$, the set of polarization basis rotations (one for each point in the upper hemisphere integration) is completely determined. In practice, source polarization may increase the sensitivity of the scattered Stokes vector components to the orientation angle ψ_{uh} and therefore require a lookup table with finer resolution than for the unpolarized case.

A more difficult problem involves the downward Faraday rotation. Were it not for the time dependence in the Faraday rotation, no additional problem would arise, since the additional rotation could be incorporated into the polarization basis transformation as an additional rotation. However, Faraday rotation is strongly time dependent, and this necessitates further approximation to be able to use a pregenerated time-independent lookup table of scattered noise. One possible approach is to approximate the downward Faraday rotation by the time-dependent value evaluated only in the specular direction. Unfortunately, in general, the scattering matrix does not commute with the downward Faraday rotation matrix, so that $\mathbf{M}_s(\Omega_a,\Omega_0)\mathbf{M}_{\mathrm{fd}}(\Omega_0,t) \neq \mathbf{M}_{\mathrm{fd}}(\Omega_0,t)\mathbf{M}_s(\Omega_a,\Omega_0)$, and thus, it is not possible to bring $\mathbf{M}_{\mathrm{fd}}(\Omega_0,t)$

outside the integral, even with the time-dependent specular approximation.

The effect of Faraday rotation is analogous to the effect of the polarization basis rotation. Without Faraday rotation, the polarization basis rotation is strictly a function of the specular location and incidence plane orientation angle ψ_{uh}, so that it will be accounted for implicitly. Unfortunately, Faraday rotation is an additional (seventh) independent variable. If, however, we neglect the portion of the ψ_{uh} dependence related to variations in the mapping from the upper hemisphere to the sky, then we can adjust ψ_{uh} by the Faraday rotation angle to obtain a new pseudo-orientation angle $\tilde{\psi}_{uh}$ that effectively accounts for Faraday rotation at the expense of properly accounting for the (possibly more subtle) effect of sky noise orientation on the upper hemisphere. According to the models considered in this paper, the maximum peak-to-peak variability (with respect to ψ_{uh}) in the scattered unpolarized signal was on order of 0.5 K; therefore, this approach may be worth consideration.

APPENDIX
GENERATION OF A REDUCED-RESOLUTION CELESTIAL MAP

Here, we describe the method that we used to generate a reduced-resolution celestial map, which conserves the energy flux of the full-resolution map.

Letting δ denote declination and α right ascension, the original discrete celestial map provides data on a grid of cells such that the brightness temperature field is piecewise constant within each cell and has the form

$$T^f_{\rm sky} = T^f_{\rm sky}\left(\delta^f_0 + (j^f-1)(\Delta\delta)^f, \alpha^f_0 + (k^f-1)(\Delta\alpha)^f\right) \tag{A1}$$

where j^f and k^f are positive integer indices that satisfy

$$1 \le j^f \le n^f_\delta \tag{A2}$$

$$1 \le k^f \le n^f_\alpha. \tag{A3}$$

Here, the grid spacing is $(\Delta\delta)^f = 0.25^\circ$ in declination and $(\Delta\alpha)^f = 0.25^\circ$ in right ascension. A reduced-resolution celestial map was produced by applying an energy-flux-conserving averaging operator $R(\cdot)$ to the original celestial map to produce a celestial noise map on a low-resolution grid $\mathbf{G}_r(j^c(\Delta\delta)^c, k^c(\Delta\alpha)^c)$, where $(\Delta\delta)^c = (2n^c+1)(\Delta\delta)^f$, and $(\Delta\alpha)^c = (2n^c+1)(\Delta\alpha)^f$. The integer rescaling factor n^c is set to 7 for this paper, which yields a 15-fold increase in grid spacing in right ascension and declination. The integer indices of the coarse grid, i.e., j^c and k^c, satisfy

$$1 \le j^c \le \frac{\left(n^f_\delta - 1\right)}{(2n^c+1)} + 1 \tag{A4}$$

$$1 \le k^c \le \frac{\left(n^f_\alpha - 1\right)}{(2n^c+1)} + 1 \tag{A5}$$

and the discrete low-resolution brightness temperature field is

$$T^c_{\rm sky}(j^c,k^c) = \frac{1}{\mathcal{N}} \sum_{j^f=j^f_0}^{j^f_1} \sum_{k^f=k^f_0}^{k^f_1} \sin\left(\delta^f_0 + j^f(\Delta\delta)^f\right) \times T^f_{\rm sky}\left(\delta^f_0 + (j^f-1)(\Delta\delta)^f, \alpha^f_0 + (k^f-1)(\Delta\alpha)^f\right) \tag{A6}$$

where $T^f_{\rm sky}$ is the (piecewise constant) fine grid brightness temperature field, and $T^c_{\rm sky}$ is the coarse grid field. The index limits of summation over the fine grid may be expressed in terms of coarse grid indices and the resolution reduction factor n^c by

$$j^f_0(j^c) = 1 + (2n^c+1)(j^c-1) - n^c \tag{A7}$$

$$j^f_1(j^c) = 1 + (2n^c+1)(j^c-1) + n^c \tag{A8}$$

$$k^f_0(k^c) = 1 + (2n^c+1)(k^c-1) - n^c \tag{A9}$$

$$k^f_1(k^c) = 1 + (2n^c+1)(k^c-1) + n^c. \tag{A10}$$

The factor

$$\mathcal{N} = \sum_{j^f=j^f_0}^{j^f_1} \sum_{k^f=k^f_0}^{k^f_1} \sin\left(\delta^f_0 + j^f(\Delta\delta)^f\right) \tag{A11}$$

is a normalization factor for the averaging operator. The first cell in the reduced grid (in both declination and right ascension) is always aligned with the first cell in each dimension in the original grid, and the celestial brightness temperature values assigned to each of the reduced-resolution grid cells is the weighted average of the brightness temperatures in all original grid cells contained within the encompassing coarse grid cell. In the averaging procedure, the weight given to a particular fine grid cell is proportional to the solid angle subtended by that cell.

ACKNOWLEDGMENT

The authors would like to thank S. Zine and D. Le Vine for contributing to the SMOS sky map generation and the anonymous reviewers for helping us improve the manuscript. The centrosymmetric weighting function used in the SMOS portion of the analysis was developed by P. Waldteufel.

REFERENCES

[1] S. H. Yueh, R. West, W. J. Wilson, F. K. Li, E. G. Njoku, and Y. Rahmat-Samii, "Error sources and feasibility for microwave remote sensing of ocean salinity," *IEEE Trans. Geosci. Remote Sens.*, vol. 39, no. 5, pp. 1049–1060, May 2001.

[2] D. M. Le Vine and S. Abraham, "Galactic noise and passive microwave remote sensing from space at L-band," *IEEE Trans. Geosci. Remote Sens.*, vol. 42, no. 1, pp. 119–129, Jan. 2004.

[3] J. Tenerelli, N. Reul, A. A. Mouche, and B. Chapron, "Earth viewing L-band radiometer sensing of sea surface scattered celestial sky radiation. Part I: General characteristics," *IEEE Trans. Geosci. Remote Sens.*, vol. 46, no. 3, pp. xxxx–xxxx, Mar. 2008.
XREF
[4] M. Sánchez-Nogales, F. Pirondini, and J. A. G. Abeytua, "Earth Explorer Mission CFI software: Mission conventions document," DEIMOS Space S.L., Madrid, Spain, Jul. 2003. Tech. Note.
[5] W. Reich, "A radio continuum survey of the northern sky at 1420 MHz—Part I," *Astron. Astrophys., Suppl. Ser.*, vol. 48, pp. 219–297, Jul. 1982.
[6] P. Reich and W. Reich, "A radio continuum survey of the northern sky at 1420 MHz—Part II," *Astron. Astrophys., Suppl. Ser.*, vol. 63, pp. 205–292, Jul. 1986.
[7] P. Reich, J. C. Testori, and W. Reich, "A radio continuum survey of the southern sky at 1420 MHz, the atlas of contour maps," *Astron. Astrophys.*, vol. 376, no. 3, pp. 861–877, Sep. 2001.
[8] J. C. Testori, P. Reich, J. A. Bava, F. R. Colomb, E. E. Hurrel, J. J. Larrarte, W. Reich, and A. J. Sanz, "A radio continuum survey of the southern sky at 1420 MHz. Observations and data reduction," *Astron. Astrophys.*, vol. 368, no. 3, pp. 1123–1132, Mar. 2001.
[9] P. M. W. Kalberla, W. B. Burton, D. Hartmann, E. M. Arnal, E. Bajaja, R. Morras, and W. G. L. Pöppel, "The Leiden/Argentine/Bonn (LAB) survey of galactic HI. Final data release of the combined LDS and IAR surveys with improved stray-radiation corrections," *Astron. Astrophys.*, vol. 440, no. 2, pp. 775–782, Sep. 2005.
[10] D. Hartmann and W. B. Burton, *Atlas of Galactic Neutral Hydrogen*. Cambridge, U.K.: Cambridge Univ. Press, 1997.
[11] E. M. Arnal, E. Bajaja, J. J. Larrarte, R. Morras, and W. G. L. Pöppel, "A high sensitivity HI survey of the sky at $\delta \leq -25°$," *Astron. Astrophys., Suppl. Ser.*, vol. 142, pp. 35–40, Feb. 2000.
[12] E. Bajaja, E. M. Arnal, J. J. Larrarte, R. Morras, W. G. L. Pöppel, and P. M. W. Kalberla, "A high sensitivity HI survey of the sky at $\delta \leq -25°$. Final data release," *Astron. Astrophys.*, vol. 440, pp. 767–773, Sep. 2005.
[13] A. Wright and R. Otrupcek, *Parkes Catalog*. Epping, Australia: Australia Telescope Nat. Facility, 1990.
[14] J. J. Condon, W. D. Cotton, E. W. Greisen, Q. F. Yin, R. A. Perley, G. B. Taylor, and J. J. Broderick, "The NRAO VLA sky survey," *Astron. J.*, vol. 115, no. 5, pp. 1693–1716, May 1998.
[15] P. Beckmann and A. Spizzichino, *The Scattering of Electromagnetic Waves From Rough Surfaces*. New York: Macmillan, 1963.
[16] A. G. Voronovich, "Small-slope approximation in wave scattering by rough surfaces," *Sov. Phys.—JETP*, vol. 62, pp. 65–70, 1985.
[17] A. Guissard, "Mueller and Kennaugh matrices in radar polarimetry," *IEEE Trans. Geosci. Remote Sens.*, vol. 32, no. 3, pp. 590–597, May 1994.
[18] C. Mätzler and P. W. Rosenkranz, "Dependence of microwave brightness temperature on bistatic surface scattering: Model functions and application to AMSU-A," *IEEE Trans. Geosci. Remote Sens.*, vol. 45, no. 7, pp. 2130–2138, Jul. 2007.
[19] D. S. S. L., Computation of the synthetic antenna directional gain as interface to L2 processor, synthetic antenna, Apr. 2005, Lisboa, Portugal: DEIMOS Space S.L. Tech. Note.
[20] P. Waldteufel and S. Zine, "Approximating the weighting function to be used in the SMOS Level 2 processor," CBSA, Toulouse, France, 2005. Tech. Rep., 32 p..
[21] J. Tournadre, B. Chapron, N. Reul, and D. C. Vandemark, "A satellite altimeter model for ocean slick detection," *J. Geophys. Res.*, vol. 111, no. C4, p. C04 004, 2006.
[22] V. N. Kudryavtsev, V. K. Makin, and B. Chapron, "Coupled sea surface-atmosphere model 2. Spectrum of short wind waves," *J. Geophys. Res.*, vol. 104, no. C4, pp. 7625–7639, 1999.
[23] M. Wolleben, T. L. Landecker, W. Reich, and R. Wielebinski, *An Absolutely Calibrated Survey of Polarized Emission From the Northern Sky at 1.4 GHz*, 2005. [Online]. Available: http://www.citebase.org/abstract?id=oai:arXiv.org:astro-ph/0510456
[24] M. Wolleben, T. L. Landecker, W. Reich, and R. Wielebinski, "An absolutely calibrated survey of polarized emission from the northern sky at 1.4 GHz—Observations and data reduction," *Astron. Astrophys.*, vol. 448, no. 1, pp. 411–424, Mar. 2006.
[25] E. Carretti, S. Poppi, W. Reich, P. Reich, E. Fuerst, G. Bernardi, S. Cortiglioni and C. Sbarra, "Deep 1.4-GHz observations of diffuse polarized emission," *Mon. Not. R. Astron. Soc.*, vol. 367, no. 1, pp 132–138, Mar. 2006. [Online] Available: http://www.citebase.org/abstract?id=oai:arXiv.org:astro-ph/0512286
[26] M. Haverkorn, B. M. Gaensler, N. M. McClure-Griffiths, J. M. Dickey, and A. J. Green, *The Southern Galactic Plane Survey: Polarized Radio Continuum Observations and Analysis*, 2006. [Online]. Available: http://www.citebase.org/abstract?id=oai:arXiv.org:astro-ph/0609010

Nicolas Reul received the B.S. degree in marine science engineering from Toulon University, Toulon, France, in 1993 and the Ph.D. degree in physics (fluid mechanics) from the University of Aix-Marseille II, Marseille, France, in 1998.

From 1999 to 2001, he was with the Department of Applied Marine Physics, Rosenstiel School of Marine and Atmospheric Science, University of Miami, Miami, FL, as a Postdoctoral Researcher in the team of Prof. M. Donelan. Since 2001, he has been a Research Scientist with the Spatial Oceanography Group, Laboratoire d'Océanographie Spatiale, Institut Français de Recherche et d'Exploitation de la Mer, Plouzané, France, where is responsible for activities concerning the SMOS satellite mission. The focus of his research program is the improvement of the understanding of the physical processes in the air–sea interface and passive/active remote sensing of the ocean surface. He has experience in applied mathematics, physical oceanography, and electromagnetic wave theory and its application to ocean remote sensing. He is a member of the European Space Agency/SMOS Science Advisory Group.

Joseph Tenerelli received the B.S. degree in atmospheric sciences from the University of Washington, Seattle, in 1994.

From 1999 to 2005, he was a Research Associate with the Rosenstiel School of Marine and Atmospheric Science, University of Miami, Miami, FL, where he was part of a team that developed a coupled atmosphere–ocean–surface wave model with vortex-following mesh refinement suitable for simulating hurricanes. Since April 2005, he has been a Research Engineer with the Laboratoire d'Océanographie Spatiale, Institut Français de Recherche et d'Exploitation de la Mer, Plouzané, France, as part of a team that is developing an algorithm for retrieving sea surface salinity from L-band radiometric measurements (the European Space Agency's Soil Moisture and Ocean Salinity project).

Nicolas Floury received the Engineering degree in telecommunication techniques from the Ecole Nationale Supérieure des Télécommunications, Paris, France, in 1993 and the Ph.D. degree in physics applied to remote sensing from the Université Paris 7, Paris, in 1999.

Since 1999, he has been with the Wave Interaction and Propagation Group, Electromagnetics and Space Environments Division, European Space Research and Technology Centre (ESTEC), European Space Agency, Noordwijk, The Netherlands. His interests are in electromagnetic modeling and signal processing applied to the study of the interaction between microwaves and natural media.

Bertrand Chapron received the B.Eng. degree from the Institut National Polytechnique de Grenoble, Grenoble, France, in 1984 and the Ph.D. degree in physics (fluid mechanics) from the University of Aix-Marseille II, Marseille, France, in 1988.

He was with the NASA Goddard Space Flight Center Wallops Flight Facility, Wallops Island, VA, for three years as a Postdoctoral Research Associate. He is currently a Research Scientist and the Head of the Spatial Oceanography Group, Laboratoire d'Océanographie Spatiale, Institut Français de Recherche et d'Exploitation de la Mer, Plouzané, France, where he is responsible for the Centre ERS Archivage et Traitement. He has been a Coinvestigator and Principal Investigator in several projects of the European Space Agency (e.g., ENVISAT and Global Navigation Satellite System), NASA, and Centre National d'Études Spatiales (e.g., TOPEX/POSEIDON and JASON). He was also responsible (with H. Johnsen of NORUT) for the ENVISAT ASAR-wave mode algorithms and scientific preparation for the ENVISAT wind and wave products. He has experience in applied mathematics, physical oceanography, and electromagnetic wave theory and its application to ocean remote sensing.